

PAPER

Large area silicon drift detectors system for high precision timed x-ray spectroscopy

To cite this article: M Miliucci *et al* 2022 *Meas. Sci. Technol.* **33** 095502

View the [article online](#) for updates and enhancements.

You may also like

- [LOFT — Large Observatory for X-ray Timing](#)
S Zane
- [Charge collection in the Silicon Drift Detectors of the ALICE experiment](#)
B Alessandro, R Bala, G Batigne et al.
- [Characterization of the ALICE Silicon Drift Detectors using an infrared laser](#)
G Batigne, S Beol , E Biolcati et al.



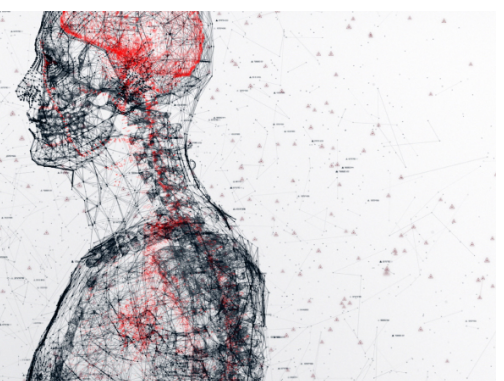
physicsworld

AI in medical physics week








20–24 June 2022

Join live presentations from leading experts
in the field of AI in medical physics.

physicsworld.com/medical-physics



Large area silicon drift detectors system for high precision timed x-ray spectroscopy

M Miliucci^{1,*} , M Iliescu^{1,*}, F Sgaramella^{1,*} , M Bazzi¹, D Bosnar² , M Bragadireanu^{1,3}, M Carminati⁴, M Cargnelli⁵, A Clozza¹, C Curceanu¹, G Deda⁴, L De Paolis¹, R Del Grande^{1,6} , C Fiorini⁴, C Guaraldo¹, M Iwasaki⁷, P King⁴, P Levi Sandri¹, J Marton⁵, P Moskal⁸ , F Napolitano¹ , S Niedźwiecki⁸, K Piscicchia^{1,9}, A Scordo¹ , H Shi^{1,5}, M Silarski⁸, D Sirghi^{1,3}, F Sirghi^{1,3}, M Skurzok^{1,8}, A Spallone¹, M Tüchler⁵, O Vazquez Doce¹ and J Zmeskal⁵

¹ Laboratori Nazionali di Frascati INFN, Via E. Fermi 54, 00044 Frascati, Italy

² Department of Physics, Faculty of Science, University of Zagreb, Zagreb, Croatia

³ Horia Hulubei National Institute of Physics and Nuclear Engineering (IFIN-HH), Măgurele, Romania

⁴ Politecnico di Milano, Dipartimento di Elettronica, Informazione e Bioingegneria and INFN Sezione di Milano, Milano, Italy

⁵ Stefan-Meyer-Institut für Subatomare Physik, Vienna, Austria

⁶ Excellence Cluster Universe, Technische Universität München, Garching, Germany

⁷ RIKEN, Tokyo, Japan

⁸ Faculty of Physics, Astronomy, and Applied Computer Science, Jagiellonian University, Łojasiewicza 11, 30-348 Kraków, Poland

⁹ Centro Ricerche Enrico Fermi—Museo Storico della Fisica e Centro Studi e Ricerche ‘Enrico Fermi’, Via Panisperna 89A, 00184, Roma, Italy

E-mail: marco.miliucci@lnf.infn.it, mihai.iliescu@lnf.infn.it and francesco.sgaramella@lnf.infn.it

Received 28 February 2022, revised 30 May 2022

Accepted for publication 9 June 2022

Published 20 June 2022



CrossMark

Abstract

The current work presents the optimization of large area silicon drift detectors developed by the SIDDHARTA-2 collaboration for high precision x-ray measurements of light exotic atom transitions. Two different radiation sources were employed in the study: an x-ray tube, for investigating the energy resolution and the charge collection efficiency of the device in the range 4000 eV–13 000 eV, and a β^- ^{90}Sr radioactive source for measuring the timing response, thus qualifying the charge drift parameters inside the semiconductor. The study reports the spectroscopic response optimization, together with the tuning of the electron dynamics for the given Silicon technology, by adjusting the applied electric field and the working temperature, which allow a good control of the device’s performances for high precision, timed x-ray spectroscopy applications.

Keywords: silicon drift detector, x-ray spectroscopy, charge dynamics, timing response, energy response

(Some figures may appear in colour only in the online journal)

* Authors to whom any correspondence should be addressed.

1. Introduction

The silicon drift detectors (SDDs) [1, 2], an evolution of the silicon drift chambers [3] position-sensing devices, combine the Silicon reverse bias p–n junction response to ionizing radiation with an innovative drift field design which minimizes the collecting anode area, resulting in a low-noise, high-rate capability device, suitable for precision x-ray measurements. The SDDs cover a wide range of applications [4–8], playing a key role in the high precision x-ray spectroscopy of light exotic atoms. In particular, the kaonic atoms spectroscopy represents a fundamental tool for probing the non-perturbative regime of quantum chromodynamics in the strangeness sector, with implications extending from particle and nuclear physics to astrophysics [9–12]. In 2009, the SDDs technology was employed for the first time by the SIDDHARTA collaboration [13], resulting in the most precise measurement of the kaonic hydrogen (K-H) fundamental level shift and width induced by the strong interaction, at the DAΦNE collider [14, 15] of Istituto Nazionale di Fisica Nucleare—Laboratori Nazionali di Frascati (INFN-LNF). Presently, the SIDDHARTA-2 collaboration is ready to perform the analogous kaonic deuterium (K-d) $2p \rightarrow 1s$ transition measurement. Theoretical calculations [16–18], estimating one order of magnitude lower yield for K-d transition with respect to the K-H one [19], were used in a Monte Carlo simulation, predicting a precision of about 30 eV for the determination of the strong interaction shift and 80 eV for the corresponding width for an integrated luminosity of 800 pb^{-1} [11]. The range of interest of SIDDHARTA-2 spans from 4000 eV to 12 000 eV, matching the SDDs' high quantum efficiency range (>85%, for a 450 μm thick Silicon wafer). Given the low expected yield (in the range of 10^{-3}), an accurate optimization of the detectors' spectroscopic response is required for the ambitious and difficult measurement of kaonic deuterium. This work presents the laboratory optimization of the SIDDHARTA-2 SDDs system using two different excitation sources (an x-ray tube and a ^{90}Sr radioactive source), for a thorough investigation of the employed technology in terms of spectroscopic response and charge drift dynamics.

2. Large area SDDs

New monolithic large area SDD arrays (figure 1) have been developed by Fondazione Bruno Kessler (Italy), together with Politecnico di Milano (Italy), LNF-INFN (Italy) and Stefan Meyer Institute (Austria), for high precision kaonic atoms spectroscopy. Each array consists of eight cells of $8 \times 8 \text{ mm}^2$ each, disposed in a 2×4 configuration on a 450 μm thick Si wafer with 1 mm dead region on the border, for an active/total area ratio higher than 80%. The wafer is glued on a ceramic carrier which provides the polarization to the SDD units and houses 8 dedicated CMOS low-noise, pulsed reset, charge sensitive cryogenic pre-amplifier (CUBE [20]), bonded to SDD anodes with a 2 mm wire. Each SDD unit is square-shaped on n^- Si bulk, with a layer of p^+ rings on one side, circling the anode and coupled to a voltage divider for shaping

the drift field, while on the opposite side, a metalized p^+ non-structured layer forms the radiation entrance window and the back contact.

The collecting anode is a small n^+ implant located at the centre of the rings, while the adjacent first p^+ ring (R1) is negatively biased. The bias progressively increases from R1 with each successive ring up to the outermost one (RN), generating a staircase potential, while the opposite equipotential surface (Back) is biased at a voltage with a fixed ratio V_{RN} / V_{Back} [21]. This configuration grants full depletion of the Si bulk and therefore a homogeneous sensitivity over the whole detector area. The simulated equipotential plots for a radial section of the detector (see section 3.1, figures 5(a) and (b)) shows a funnel-shape potential with a diagonal maximum on which the resulting drift field channels the radiation-generated electrons from both back side and ring side, focusing them on the n^+ collecting anode, while the generated holes are collected by the reverse-biased p^+ implanted regions (back and rings). The small capacitance anode minimizes the effect of the preamplifier series noise, resulting in a large area device with low electronic noise and high-rate capability.

2.1. SDD optimization experimental setup

The SDD array under study was installed inside a 500 mm \times 300 mm \times 300 mm Aluminium vacuum chamber with a 150 μm thick, 60 mm diameter Mylar window on top, two vacuum pipes on the side for the pumping system and cryogenics and vacuum feed-troughs for slow controls, detector bias and signals (figure 2). The device is mounted on a cold finger connected to the cooling head of a closed-cycle expansion cryostat. An 801 s^{-1} dry turbo molecular pump and a dry multistage scroll pump grant the high vacuum ($P = 5 \times 10^{-7}$ mbar) required for thermal insulation and for preventing contaminants and ice condensation on detector's surface. The pressure is read by a full-range vacuum gauge. The device is cooled down at a mean rate of 1 K min^{-1} and a proportional–integral–derivative feedback heater allows fixing the set point value between 100 K and 250 K, with a stability of 0.2 K.

A set of resistance temperature detectors placed from the detector vicinity up to the cooling head, provide the temperature readings.

Two configurations, matching the two radiation sources, as shown in the figures 2(a) and (b), were used to determine the SDDs' properties. The first one, illustrated in figure 2(a) was dedicated to the SDDs' energy response in the range 4–13 keV. A target made of strips of Titanium, Iron, Copper, and epoxy-encapsulated Potassium Bromine was attached on an Aluminium support and positioned obliquely at 45° in front of the Mylar window. An x-ray tube (Oxford Instruments HXR 55-50-01) placed 100 mm away from the target provides a divergent beam, parallel to the entry window. When operated at 23 kV and 10 μA , the tube irradiates the target elements, inducing their x-ray fluorescence, subsequent to the photoelectric excitation. The $K\alpha$ and $K\beta$ transition photons are detected for all the target elements, covering the above-mentioned range, while delivering a flux of about 1 KHz on each detector surface. The 45° positioning of the target avoids direct shining

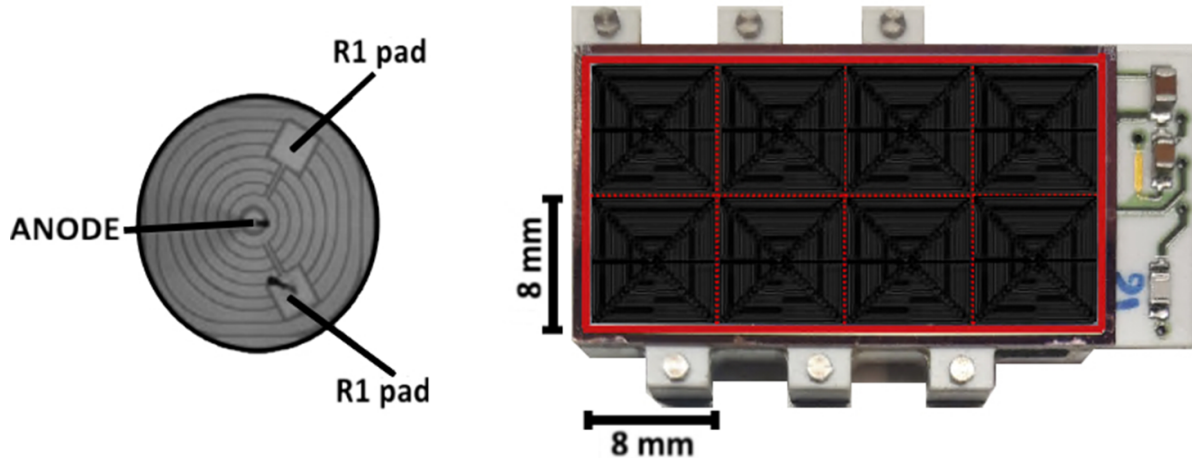


Figure 1. Left: detail of the single cell rings shape. Right: picture of the SIDDHARTA-2 silicon drift detectors 2×4 array screwed on the aluminium block. The red rectangle defines the active area of the device (5.12 cm^2) given by the eight cells of 0.64 cm^2 each.

of the x-ray tube through the window, while maximizing the ratio between the detected fluorescent photons and the incident activation beam.

The signals coming from the detectors are buffered by CUBE, installed on the detector ceramics a few mm from the anode, then processed by a dedicated linear low-noise front end ASIC (SFERA [22, 23]) and by a custom-build DAQ, based on National Instruments FPGA boards and ADCs. The signal processing chain has demonstrated the ability to handle high rates of x-ray photons, while preserving the integrity of the information even when the detectors are operated under the high background environment of a particle collider [24].

The configuration shown in the figure 2(b) was used to extend the SDDs study to their time response, using a β^- ^{90}Sr source. The source generates x-ray lines by fluorescent excitation of the multi-element (Fe, Cu) target. In addition to the energy deposited by the photons, the β^- source allows extracting the timing information, using as reference a fast pulse provided by a thin scintillator through which the emitted electrons pass before hitting the target. Given the low β^- fluorescence activation rate (below 2 Hz) and the required time resolution, a second DAQ chain, equipped with 1 Gs s^{-1} Flash ADCs (ten times better time resolution than the standard ASIC-FPGA-ADC one) was used. The CUBE-buffered x-ray signals, reproducing the anode charging, are seen as a saw-step on the leakage ramp and were processed by a three-line fit procedure described in [25], allowing to record both the energy and timing information for each detected event.

3. The spectroscopic response

3.1. Energy response

The study of the SDDs' energy response, as a function of the bias voltages, has been performed for optimizing the drift field parameters, by comparing the spectroscopy results with the simulation of the collection path efficiency. An external DC power supply provided the main voltage (V_D), and a voltage

divider sets the V_{RN} at $0.75 \cdot V_D$ and V_{Back} at $0.66 \cdot V_{RN}$, while keeping fixed the V_{R1} at -15.0 V .

For convenience, although bias voltages are negative (for drifting electrons towards the anode) only the absolute values will be reported in the following.

The energy response of the device to a specific fluorescence line is described by a Gaussian and a low energy tail, the last related to inefficiencies in charge collection. The overall fit equation consists of a sum of Gaussians and tail functions [26–28] for the fluorescence peaks and a first-degree polynomial for the background. The fit procedure has been performed using MINUIT, through MIGRAD minimizations. As an example, figure 3 shows the fitted spectrum, in ADC channels, obtained at a temperature of $122.1 \pm 0.2 \text{ K}$ under an applied V_D of $140.0 \pm 0.1 \text{ V}$, by the excitation of the multi-element (Ti–Fe–Cu–Br) target with the x-ray tube, operated at 23 kV and $10 \mu\text{A}$.

The Gaussian peak positions and their widths were used to extract the linearity and the energy resolution of the detector. The response of the system has been studied as a function of the drift voltage (V_D), in the range between $95.0 \pm 0.1 \text{ V}$ and $180.0 \pm 0.1 \text{ V}$.

Only the $K\alpha$ peaks were included in the calibration procedure, due to their higher signal-to-background ratio. To determine the gain of the system in terms of eV channel^{-1} , the positions of the $K\alpha$ peaks were plotted as a function of the reference tabulated energies and a first-degree polynomial has been used to fit the calibration points. The residuals are below $\pm 3 \text{ eV}$ for the full operating range of drift voltages, confirming the linear response of system, as previously shown [24, 29].

The resolution dependence on the drift field shows a relatively wide-range stable figure for values of V_D between $100.0 \pm 0.1 \text{ V}$ and $140.0 \pm 0.1 \text{ V}$. Figure 4 left shows the overlap of the spectra acquired at $V_D = 100.0 \pm 0.1 \text{ V}$, $140.0 \pm 0.1 \text{ V}$ and $180.0 \pm 0.1 \text{ V}$, while on the right, the resolution values are plotted against V_D , displaying a consistent broadening of the peaks at $180.0 \pm 0.1 \text{ V}$. Since the spectra were acquired in the same experimental conditions, the intrinsic statistical

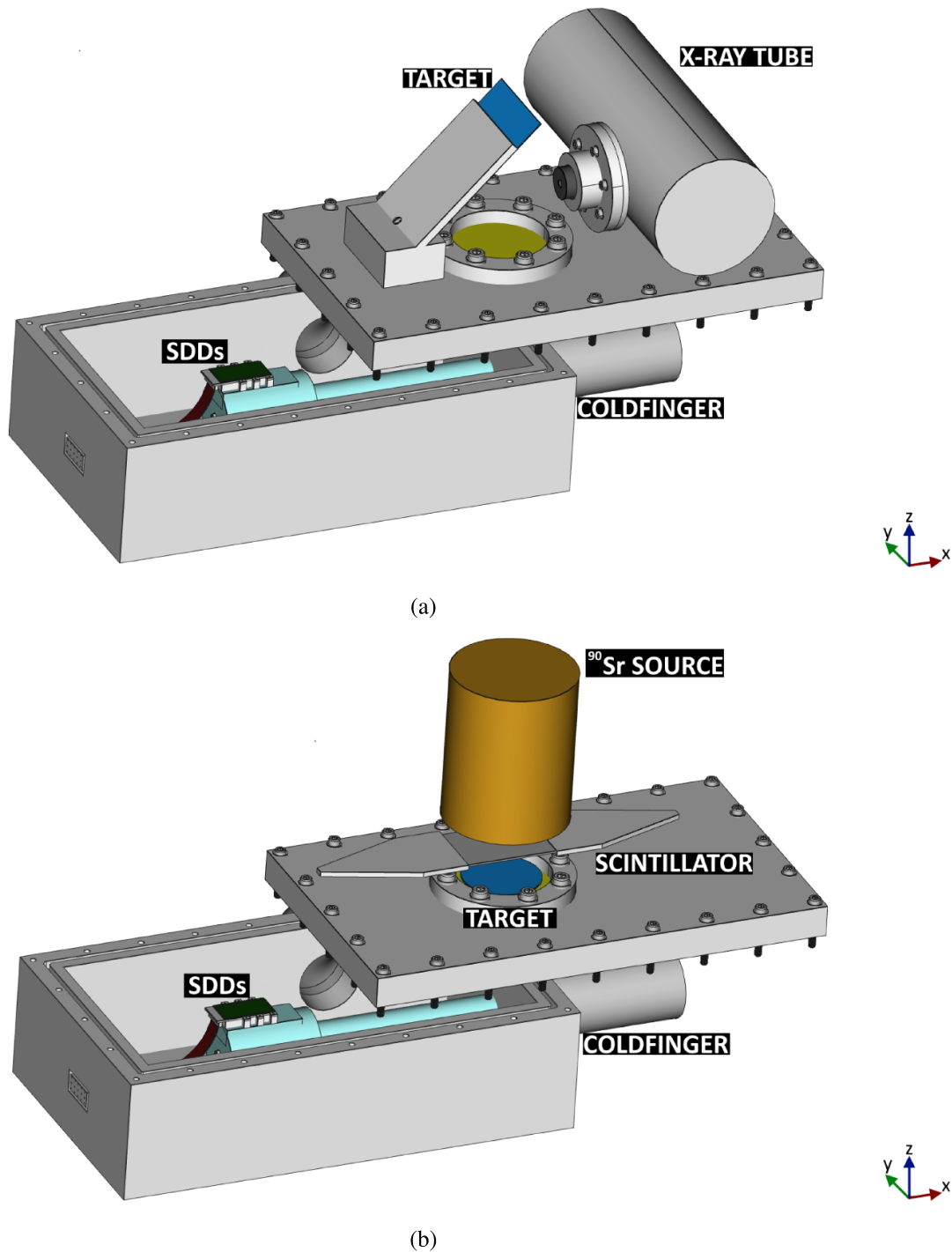


Figure 2. Drawing of the setup configuration for the optimization of the SDD operational regime through x-ray tube (a) and ⁹⁰Sr source (b) measurements.

fluctuations ($FWHM_{intr.}$) and the electronic noise contribution ($FWHM_{noise}$) cannot explain the resolution blowup, so a third component, related to the incomplete charge collection effect ($FWHM_{c.c.}$) [30], must be considered.

Hence, the equation for the energy resolution consists of three terms:

$$FWHM_{TOT}^2 = FWHM_{intr.}^2 + FWHM_{noise}^2 + FWHM_{c.c.}^2 \quad (1)$$

A study of the charge collection efficiency has been performed, combining the statistical analysis with numerical simulations. The number of events related to the incomplete charge collection, estimated by the integral of the Tail function [26–28] obtained by fitting the Fe $K\alpha$ peak, was compared to the integral of the Gaussian component. A qualitative support of the analysis was provided by the simulation of the electric potential and the corresponding charge transport inside the SDD, showing the electrons’ and holes’ drift path variations

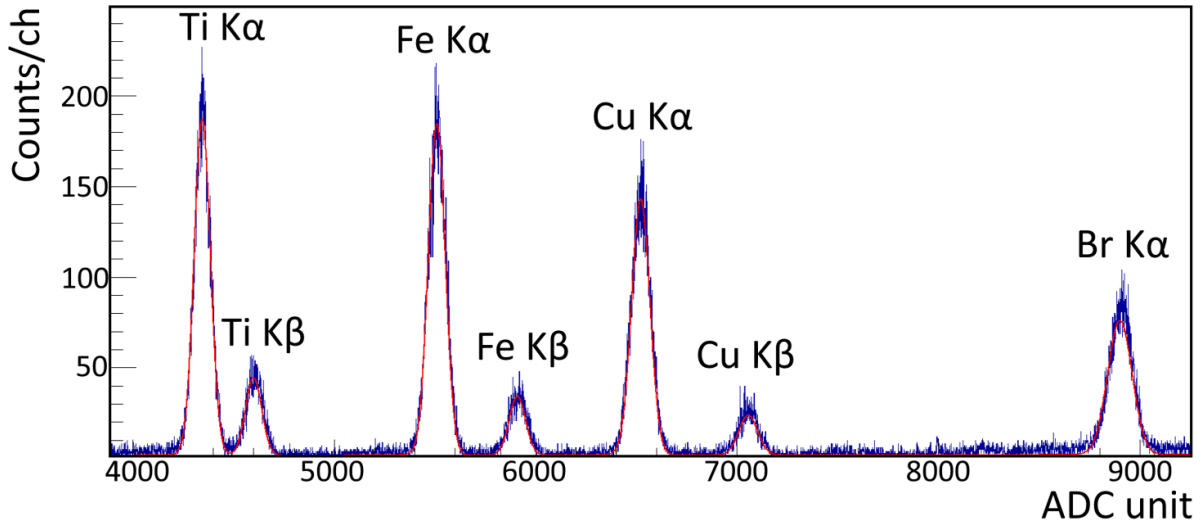


Figure 3. Fit of the SDD spectrum obtained at $T = 122.1 \pm 0.2$ K and $V_D = 140.0 \pm 0.1$ V.

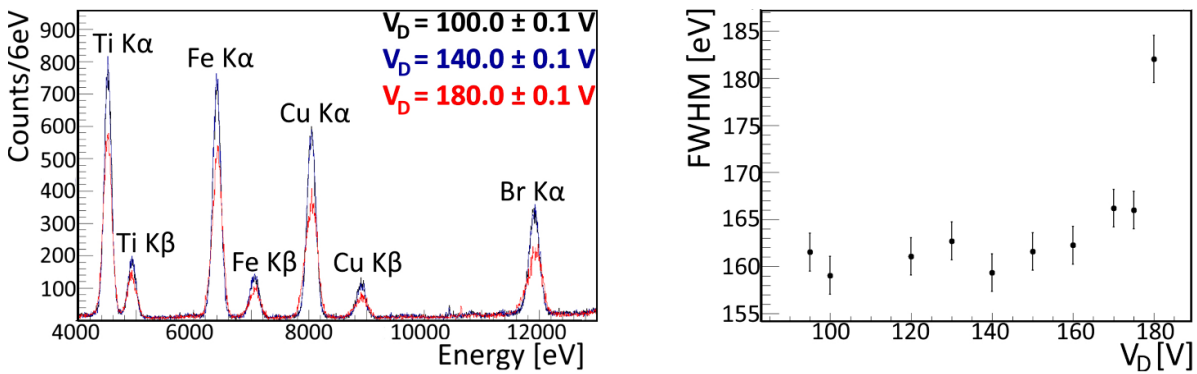


Figure 4. Left: the overlap of the spectra acquired at $V_D = 100.0 \pm 0.1$ V, 140.0 ± 0.1 V, 180.0 ± 0.1 V with the x-ray tube at 23 kV–10 μ A; Right: SDD energy resolution at Fe $K\alpha$ line in the range from 95.0 ± 0.1 to 180.0 ± 0.1 V.

with the applied bias. The simulations, based on the numerical solutions of Poisson/Laplace equations, used the ROOT-KDetSim shared libraries developed by [31–33]. The drift path of the generated electron–hole pairs was numerically reconstructed in steps, by applying the equations:

$$\Delta r = v(r) \cdot \Delta t \quad (2)$$

$$v(r) = \mu \cdot E(r) \quad (3)$$

where E is the electric field, v and μ the velocity and mobility of the charge, respectively.

Figure 5 compares the Gauss and Tail contributions of the $K\alpha$ Fe peak for drift voltages V_D of 100.0 ± 0.1 V, 140.0 ± 0.1 V and 180.0 ± 0.1 V. The total number of events (figures 5(a) and (b), left) for $V_D = 100.0 \pm 0.1$ V and $V_D = 140.0 \pm 0.1$ V is the same, within the statistical error, and so is the ratio between the Tail and the Gauss components, both lower than 1%. Consistently, the figures 5(a) and (b) (right) show the diagonal transport field, crossing the equipotential surfaces inside the device, and efficiently focusing the electrons to the anode, in both cases. Increasing V_D to 180.0 ± 0.1 V, a reduced number of charges collected at anode is observed, demonstrated

by both the lower amplitude of the fluorescence peaks for the calibrated spectrum (figure 4 left) and the downward shift of the peak position in the raw data (figure 5(c) left). Furthermore, the number of Tail events is significantly higher and the ‘Tail to Gauss ratio’ rises up to 5%, as shown in figure 5(c), left. The related simulation on the right confirms the experimental observation, showing that a drift field created by an applied voltage of 180.0 ± 0.1 V is unable to efficiently focus the electrons to the anode.

The event statistics in terms of Tail over Gauss ratio (H_T / H_G) for all the spectra obtained by varying the drift field in the range 95.0 ± 0.1 V– 180.0 ± 0.1 V, are summarized in figure 6. The energy resolution of the Fe $K\alpha$ line (figure 4 right) is consistent with the tail behavior and remains stable in the V_D range from 100.0 ± 0.1 V to 175.0 ± 0.1 V, with values compatible with other low-noise Silicon x-ray detectors, while a worsening is observed at 180.0 ± 0.1 V.

In conclusion, it has been demonstrated that the SDDs have a wide drift field operating range, so that the SIDDHARTA-2 SDDs drift field voltage will be set at 140.0 ± 0.1 V, in the middle of the good operation range, without drawbacks in terms of the detector’s energy response, even for a common polarization of the eight units.

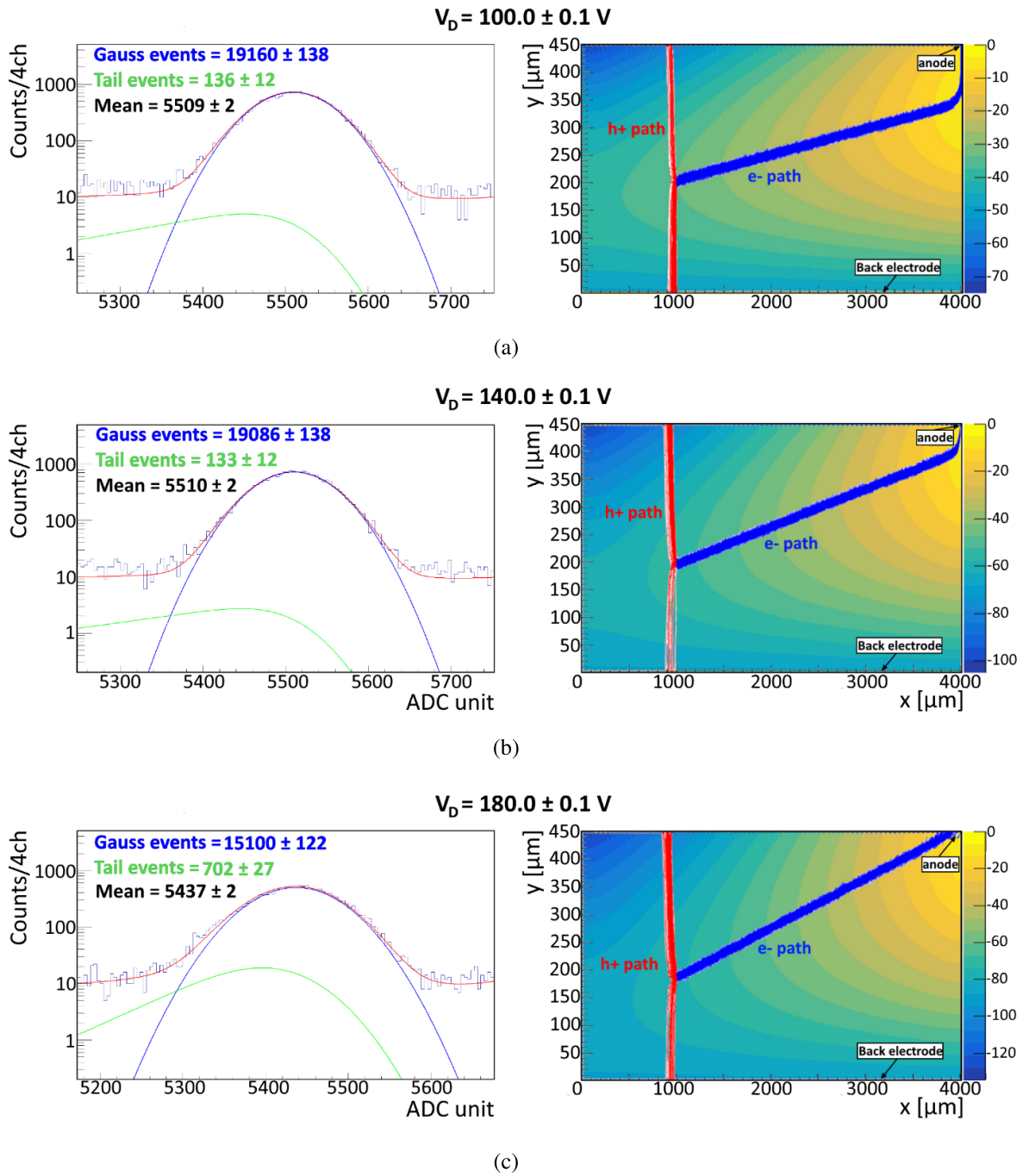


Figure 5. Left: evaluation of Tail events and Gauss events. Right: equipotential lines in a cross section of the SDD from the right edge of the detector to the center, where the anode is placed (top-right). Drift paths of electrons and holes in blue and red, respectively. Comparison between: (a) $V_D = 100.0 \pm 0.1$ V; (b) $V_D = 140.0 \pm 0.1$ V; (c) $V_D = 180.0 \pm 0.1$ V.

3.2. Timing response

The response time of the device, defined as the time interval between the charge creation and its anode collection, varies with the position of the interaction point, with the drift field and with the intrinsic properties of the semiconductor. Given the small transverse distances, limited by the device thickness (about 20 times smaller than the SDD side), one can count as the main collection path the radial distance d from

the generation point to the anode, corresponding to an average drift time defined as:

$$t_{\text{drift}} = \frac{d}{v_{\text{drift}}} = \frac{d}{\mu \cdot E} \quad (4)$$

where v_{drift} is the drift velocity of the charge carriers, μ is the intrinsic mobility and E is the applied electric field. The charge diffusion during the transport of a well-localized charge

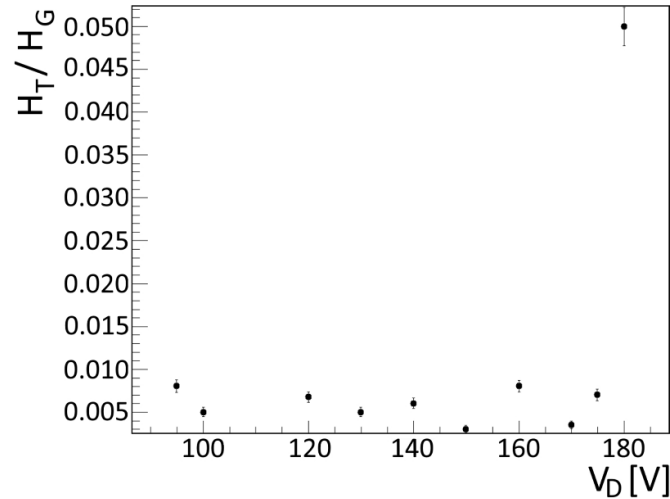


Figure 6. SDD energy response summary at different voltages in terms of the H_T / H_G .

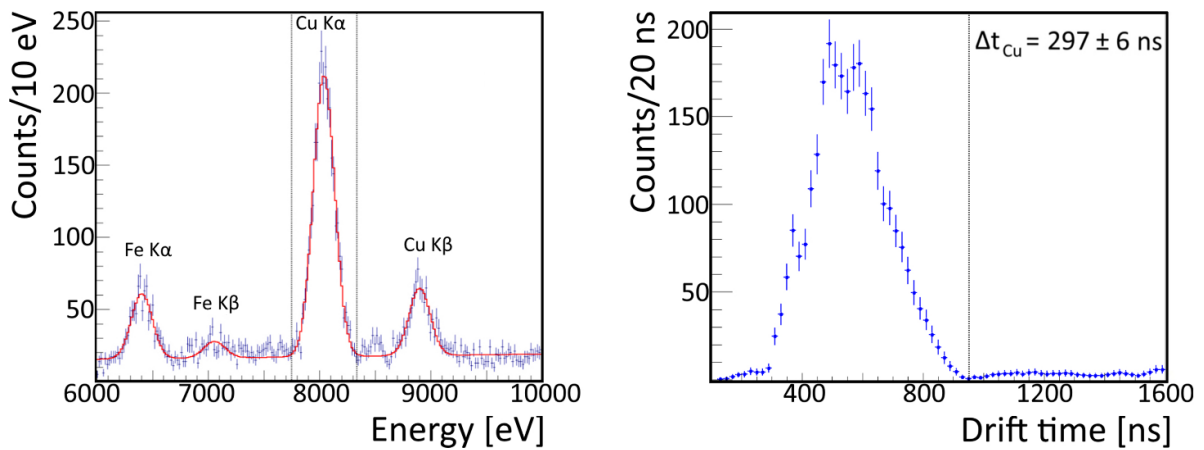


Figure 7. Left: fit of the calibrated spectrum resulting from the photons detected by a single SDD using the ^{90}Sr source to excite the Fe–Cu target. Black dotted lines define the 3σ interval around the Cu $K\alpha$ peak. Right: timing distribution of Cu $K\alpha$ peak events (black dots line defines the cut threshold). The measured timing resolution at $199.8 \pm 0.2 \text{ K}$ is $297 \pm 6 \text{ ns}$.

packet, produced by the point-like photoelectric effect has a small contribution ($\simeq 10^{-8} \text{ s}$) to the total collection time [20].

Therefore, the time resolution of the detector is mainly given by the drift time distribution of the charge packets created by hits scattered all over the device area and, thus, it depends on the geometry of the detector, on the voltage applied and on the mobility. Having fixed the detector size according to the experiment needs and the bias voltage as described above, the subsequent study was oriented to the only accessible parameter which controls the mobility, i.e. the temperature.

A β^- ^{90}Sr source was used to excite the fluorescence x-ray lines on the Fe–Cu target (figure 2(b)). A 1.5 mm thick scintillator, placed between the source and the target and read by two Silicon Photomultipliers in coincidence mode, is traversed by the emitted electrons and provides the reference trigger.

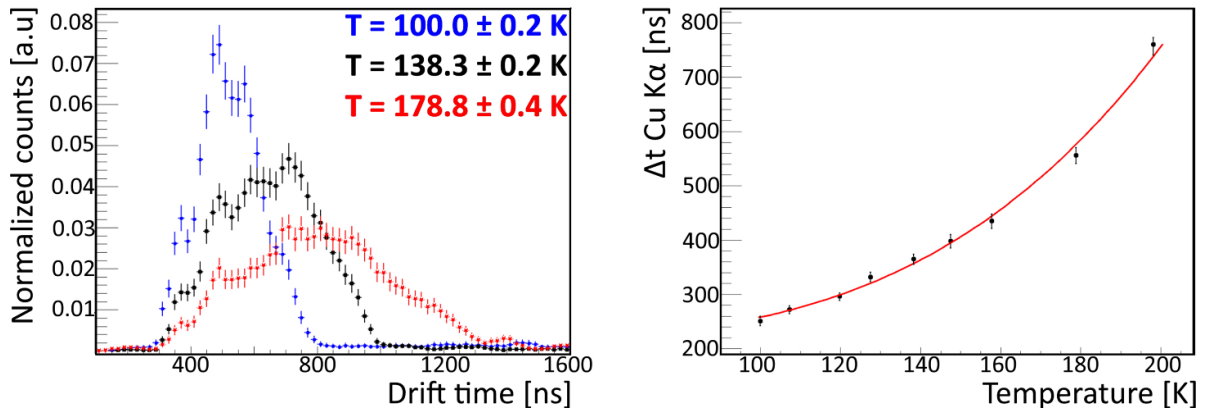
The activation rate is many orders of magnitude below the one obtained with the x-ray tube and, therefore, the statistics is reduced and so is the signal to background ratio. Given the low rate and the required time accuracy, the data was acquired

through a Flash ADC sampling the waveform at 1 Gs s^{-1} . Figure 7 left shows the energy spectrum at $T = 119.8 \pm 0.2 \text{ K}$, together with the fit function, used to define a 3σ selection around the Cu $K\alpha$ peak. The subsequent analysis refers only to the Cu $K\alpha$ line as it allows a more accurate range selection, given the higher signal over background ratio. Consequently, the time resolution measurement counts the photons detected within the chosen 3σ energy range. The associated drift time distribution is plotted in the figure 7 right. The time spectrum corresponds to an overall window of $1.6 \mu\text{s}$ ($1 \text{ ns channel}^{-1}$), equivalent to the whole Flash ADC sampling buffer for the given rate. The time reference is provided by the scintillator, while the acquisition is triggered when both scintillator and SDD provided a signal. The peak's shape reflects the square geometry of the detector, while the tail distribution is due to the accidental events coming from the high-rate β^- source and was, therefore, excluded from analysis with a cut, as indicated in figure 7 right.

The cut was selected such that the number of counted events to correspond to 3σ equivalent of the timing peak distribution

Table 1. Summary of the SDD timing response at different temperatures: ± 20 ns variation to the 3σ threshold defines the systematic errors.

Temperature (K)	δT (K)	Entries	Δt Cu $K\alpha$ (ns)	Stat. (ns)	Syst. (+) (ns)	Syst. (–) (ns)
100.0	0.2	2996	250	5	2	–1
107.3	0.1	2327	273	6	0	–1
119.8	0.2	2907	297	6	1	0
127.5	0.3	2976	332	6	1	–1
138.3	0.2	3076	361	7	1	–1
147.5	0.2	1585	400	10	1	–1
157.8	0.2	2358	435	9	2	–2
178.8	0.4	2870	556	10	1	–1
198.1	0.2	3590	761	13	0	0

**Figure 8.** Left: SDD timing distributions, normalized to the total number of collected events, overlapped at 100.0 ± 0.2 K (blue dots)— 138.3 ± 0.2 K (black squares) and 178.8 ± 0.4 K (red stars). Right: SDD time resolutions at Cu $K\alpha$ line in the range from 100 K to 200 K (red line corresponds to the equation (7) used for the fit).

(black dotted line). Given the specific time distribution related to the intrinsic geometry and drift field of the unit, the time resolution and its statistical error are defined in terms of root mean square (RMS) of the time spectrum as follows:

$$\Delta t_{\text{Cu}} = 2.35 \cdot \text{RMS} \quad (5)$$

$$\delta(\Delta t_{\text{Cu}}) = \frac{2.35 \cdot \text{RMS}}{\sqrt{\text{entries}}}. \quad (6)$$

Having set the drift voltage at 140.0 ± 0.1 V as a result of the optimization discussed in section 3.1, the dynamics of the majority carriers (electrons) was reflected in the time response of the device as a function of temperature.

Table 1 summarizes the SDD time resolution for the Cu $K\alpha$ line at different temperatures, including the systematic errors due to the threshold cut variations on the drift time histogram. Figure 8 left compares the response time distributions at 100.0 ± 0.2 K, 138.8 ± 0.2 K and 178.8 ± 0.4 K for the Cu $K\alpha$ line, normalized to the total number of collected events. The three histograms are substantially different, showing the widening of the drift time (defined as the width of the distribution), with the temperature increment, coherent with the gradual reduction of the electrons' mobility.

Since this intrinsic characteristic of the bulk follows a power-law trend with the temperature, the SDDs' response,

reflecting the electron travel time, can be expressed as a function of the carriers' mobility. Integrating the equations (2) and (3), the best fit function for the scatter plot in figure 8 right is the following:

$$\Delta t_{\text{Cu}} = a \cdot \left(\frac{T}{T_0}\right)^n + c, \quad (7)$$

where T_0 is 300 K, while a and c are constants depending on the material and on the applied bias. The reduced chi square ($\chi^2 = 1.16$), with residuals within ± 20 ns, shows the correct transport modelling, directly correlating the SDDs' time resolution to the mobility of the majority carriers.

Given that, it is possible to control the time response of the detector between 100 K and 200 K. Furthermore, this feature is fundamental for a device performing precision x-ray spectroscopy in a high radiation environment, allowing for the selection of a narrow time window for the triggered events under study and the rejection of the asynchronous accelerator background. For the SIDDHARTA-2 experiment the MC simulations [11] estimate a significant improvement in the background rejection capability by using the new SDD detectors, with a time resolution in the range 300–400 ns, to be compared with the previous devices, characterized by resolutions between 800 and 900 ns [11].

4. Conclusions

The optimization of the operational regime of SIDDHARTA-2's experiment large area SDD arrays presented in this work is based on the study of spectroscopic and time response of the devices, fundamental for the high precision measurements of kaonic atoms at the DAΦNE collider of INFN-LNF.

The energy resolution of the detectors proved to be stable over a wide range of applied drift fields, allowing to set an optimal bias voltage not sensitive to small variations in individual array response. The electric field is limited to a maximum operating value by the anode charge collection inefficiency, which can be derived from the shape of the peaks, showing, above a certain bias, a significant increment of the Tail component with respect to the main Gaussian contribution, thus worsening the energy resolution. The SDDs time response in the range from 100 K to 200 K follows a power law trend in temperature, showing the charge packet drift time variation associated to the temperature effect on the mobility.

The optimization of the SDDs functioning, supported by numerical simulations, is important for performing high precision x-ray spectroscopy measurements in the radiation environment of a collider, as well as in all those applications requiring high performances in terms of energy and timing resolutions.

Data availability statement

The data that support the findings of this study are available upon reasonable request from the authors.

Acknowledgments

The authors acknowledge C Capoccia from INFN-LNF and H Schneider, L Stohwasser, and D Pristauz Telsnigg from Stefan-Meyer-Institut für Subatomare Physik for their fundamental contribution in designing and building the SIDDHARTA-2 setup. We thank as well the DAΦNE staff for the excellent working conditions and permanent support.

Fundings

Part of this work was supported by the Austrian Science Fund (FWF): P24756-N20 and P33037-N; the Croatian Science Foundation under the Project IP-2018-01-8570; EU STRONG-2020 project (Grant Agreement No. 824093), the EU Horizon 2020 Project under the MSCA G.A. 754496, the Polish Ministry of Science and Higher Education Grant No. 7150/E-338/M/2018 and the Foundational Questions Institute and Fetzer Franklin Fund, a donor advised fund of Silicon Valley Community Foundation (Grant No. FQXi-RFP-CPW-2008).

ORCID iDs

M Miliucci [ID](https://orcid.org/0000-0002-2315-2379) <https://orcid.org/0000-0002-2315-2379>
 F Sgaramella [ID](https://orcid.org/0000-0002-0011-8864) <https://orcid.org/0000-0002-0011-8864>
 D Bosnar [ID](https://orcid.org/0000-0003-4784-393X) <https://orcid.org/0000-0003-4784-393X>
 R Del Grande [ID](https://orcid.org/0000-0002-7599-2716) <https://orcid.org/0000-0002-7599-2716>
 P Moskal [ID](https://orcid.org/0000-0002-4229-3548) <https://orcid.org/0000-0002-4229-3548>
 F Napolitano [ID](https://orcid.org/0000-0002-8686-5923) <https://orcid.org/0000-0002-8686-5923>
 A Scordo [ID](https://orcid.org/0000-0002-7703-7050) <https://orcid.org/0000-0002-7703-7050>

References

- [1] Lechner P *et al* 1996 Silicon drift detectors for high resolution room temperature x-ray spectroscopy *Nucl. Instrum. Methods Phys. Res. A* **377** 346–51
- [2] Lechner P *et al* 2001 Silicon drift detectors for high count rate x-ray spectroscopy at room temperature *Nucl. Instrum. Methods Phys. Res. A* **458** 281–7
- [3] Gatti E and Rehak P 1984 Semiconductor drift chamber—an application of a novel charge transport scheme *Nucl. Instrum. Methods Phys. Res.* **225** 608–14
- [4] Newbury D and Ritchie N 2015 Performing elemental microanalysis with high accuracy and high precision by scanning electron microscopy/silicon drift detector energy-dispersive x-ray spectrometry (SEM/SDD-EDS) *J. Mater. Sci.* **50** 493–518
- [5] Campana R *et al* 2011 Imaging performance of a large-area silicon drift detector for x-ray astronomy *Nucl. Instrum. Methods Phys. Res. A* **633** 22–30
- [6] Fiorini C, Gola A, Longoni A, Zanchi M, Restelli A, Perotti F, Lechner P, Soltau H and Strüder L 2006 A large-area monolithic array of silicon drift detectors for medical imaging *Nucl. Instrum. Methods Phys. Res. A* **568** 96–100
- [7] Fiorini C *et al* 2012 The HICAM gamma camera *IEEE Trans. Nucl. Sci.* **59** 537–44
- [8] Bazzi M *et al* 2011 Performance of silicon-drift detectors in kaonic atom x-ray measurements *Nucl. Instrum. Methods Phys. Res. A* **628** 264–7
- [9] Merafina M, Saturni F G, Curceanu C, Del Grande R and Piscicchia K 2020 Self-gravitating strange dark matter halos around galaxies *Phys. Rev. D* **102** 083015
- [10] Curceanu C *et al* 2020 Kaonic atoms to investigate global symmetry breaking *Symmetry* **12** 547
- [11] Curceanu C *et al* 2019 The modern era of light kaonic atom experiments *Rev. Mod. Phys.* **91** 025006
- [12] De Pietri R, Drago A, Feo A, Pagliara G, Pasquali M, Traversi S and Wiktorowicz G 2019 Merger of compact stars in the two-families scenario *Astrophys. J.* **881** 122
- [13] Bazzi M *et al* 2011 A new measurement of kaonic hydrogen x-rays *Phys. Lett. B* **704** 113–7
- [14] Milardi C *et al* 2018 Preparation activity for the Siddharta-2 run at DAΦNE *9th Int. Particle Accelerator Conf.*
- [15] Zobov M *et al* 2010 Test of “crab-waist” collisions at the DAΦNE Φ factory *Phys. Rev. Lett.* **104** 174801
- [16] Doring M and Meißner U-G 2011 Kaon-nucleon scattering lengths from kaonic deuterium experiments revisited *Phys. Lett. B* **704** 663
- [17] Shevchenko N 2012 Near-threshold K^-d scattering and properties of kaonic deuterium *Nucl. Phys. A* **890–891** 50
- [18] Hoshino T, Ohnishi S, Horiuchi W, Hyodo T and Weise W 2017 Constraining the $\bar{K}N$ interaction from the 1S level shift of kaonic deuterium *Phys. Rev. C* **96** 045204

- [19] Bazzi M *et al* (SIDDHARTA) 2013 Preliminary study of kaonic deuterium x-rays by the SIDDHARTA experiment at DAΦNE *Nucl. Phys. A* **907** 69–77
- [20] Bombelli L, Fiorini C, Frizzi T, Nava R, Greppi A and Longoni A 2010 Low-noise CMOS charge preamplifier for x-ray spectroscopy detectors *IEEE Nuclear Science Symp. Medical Imaging Conf.* pp 135–8
- [21] Fiorini C, Longoni A and Lechner P 2000 Single-side biasing of silicon drift detectors with homogeneous light-entrance window *IEEE Trans. Nucl. Sci.* **47** 1691–5
- [22] Quaglia R, Schembari F, Bellotti G, Butt A D, Fiorini C, Bombelli L, Giacomini G, Ficorella F, Piemonte C and Zorzi N 2016 Development of arrays of silicon drift detectors and readout ASIC for the SIDDHARTA experiment *Nucl. Instrum. Methods Phys. Res. A* **824** 449–51
- [23] Schembari F, Quaglia R, Bellotti G and Fiorini C 2016 SFERA: an integrated circuit for the readout of x and γ -ray detectors *IEEE Trans. Nucl. Sci.* **63** 1797
- [24] Miliucci M *et al* 2021 Silicon drift detectors system for high-precision light kaonic atoms spectroscopy *Meas. Sci. Technol.* **32** 095501
- [25] Iliescu M A, Miliucci M, Amirkhani A, Bazzi M, Curceanu C, Fiorini C, Sirghi F C and Zmeskal J 2021 Reducing the MIPs charge-sharing background in x-ray spectroscopic SDD arrays *IEEE Trans. Instrum. Meas.* **70** 9507807
- [26] Campbell J L 1990 X-ray spectrometers for PIXE *Nucl. Instrum. Methods Phys. Res. B* **49** 115–25
- [27] Campbell J L and Maxwell J A 1997 A cautionary note on the use of the hypermet tailing function in x-ray spectrometry with Si(Li) detectors *Nucl. Instrum. Methods Phys. Res. B* **129** 297–9
- [28] Gysel M, Lemberge P and Van Espen P 2003 Implementation of a spectrum fitting procedure using a robust peak model *X-Ray Spectrom.* **32** 434–41
- [29] Miliucci M, Iliescu M, Amirkhani A, Bazzi M, Curceanu C, Fiorini C, Scordo A, Sirghi F and Zmeskal J 2019 Energy response of silicon drift detectors for kaonic atom precision measurements *Condens. Matter* **4** 31
- [30] Perotti F and Fiorini C 1999 Observed energy dependence of Fano factor in silicon at hard x-ray energies *Nucl. Instrum. Methods Phys. Res. A* **423** 356–63
- [31] Kramberger G 2001 Signal development in irradiated silicon detectors *PhD Thesis* University of Ljubljana
- [32] Kramberger G, Cindro V, Mandic I, Mikuz M and Zavrtanik M 2002 Influence of trapping on silicon microstrip detector design and performance *IEEE Trans. Nucl. Sci.* **49** 1717–23
- [33] Kramberger G, Cindro V and Mikuz M 2001 Signals in non-irradiated and irradiated single-sided silicon detectors *Nucl. Instrum. Methods Phys. Res. A* **457** 550–7